

Quantum Finite-Size Effects in Graphene Plasmons

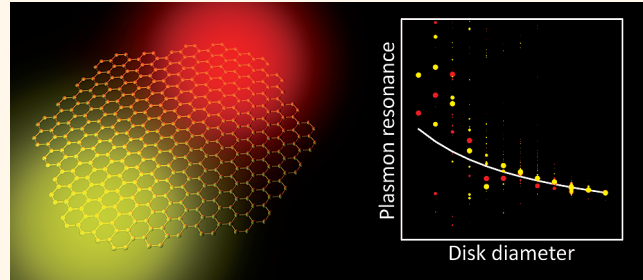
Sukosin Thongrattanasiri, Alejandro Manjavacas, and F. Javier García de Abajo^{†,*}

IQFR-CSIC, Serrano 119, 28006 Madrid, Spain. [†]Present address: Currently on sabbatical at Optoelectronics Research Centre, University of Southampton, Southampton SO17 1BJ, U.K.

The collective excitations of conduction electrons in nanostructured metals known as plasmons are currently finding application in areas as diverse as ultrasensitive biosensing,^{1–3} cancer therapy,^{4,5} photodetection,⁶ and improved photovoltaics,^{7,8} out of which commercial devices are either available or expected to be released in the short term. Additionally, plasmons are being investigated for potential use in optical signal processing,⁹ improved nonlinear response,^{10,11} and quantum information devices.^{12,13} These fields are fueled by the ability of plasmons (i) to confine electromagnetic energy down to truly nanometer scales, well below the wavelength scale imposed by the diffraction limit, and (ii) to consequently enhance the light intensity relative to externally supplied illumination.¹⁴ However, as powerful as plasmons may seem, further exploitation of these excitations is being hampered by their limited lifetimes, typically of a few tens of optical cycles in confined configurations (e.g., $\sim 10^{-13}$ s within the near-infrared). Additionally, plasmons are difficult to control without producing structural changes in the materials in which they are trapped.

In this context, the high degree of confinement and long lifetimes of plasmons in graphene compared to conventional metal plasmons¹⁵ have stimulated intense experimental and theoretical efforts to study these collective excitations, partly triggered by the prospect of applications to metamaterials,^{16,17} photodetection,^{18,19} and quantum optics.²⁰ Besides its high degree of crystallinity compared to noble metals, graphene offers the advantage of being easily tunable via electrostatic gating, whereby a net density of electrons or holes is created in the carbon sheet to screen the perpendicular dc electric field produced by a nearby electrode, typically placed in a backgate configuration. This provides a convenient way to tune the Fermi energy up to >1 eV^{21,22} and

ABSTRACT



Graphene plasmons are emerging as an alternative solution to noble metal plasmons, adding the advantages of tunability *via* electrostatic doping and long lifetimes. These excitations have been so far described using classical electrodynamics, with the carbon layer represented by a local conductivity. However, the question remains, how accurately is such a classical description representing graphene? What is the minimum size for which nonlocal and quantum finite-size effects can be ignored in the plasmons of small graphene structures? Here, we provide a clear answer to these questions by performing first-principles calculations of the optical response of doped nanostructured graphene obtained from a tight-binding model for the electronic structure and the random-phase approximation for the dielectric response. The resulting plasmon energies are in good agreement with classical local electromagnetic theory down to ~ 10 nm sizes, below which plasmons split into several resonances that emphasize the molecular character of the carbon structures and the quantum nature of their optical excitations. Additionally, finite-size effects produce substantial plasmon broadening compared to homogeneous graphene up to sizes well above 20 nm in nanodisks and 10 nm in nanoribbons. The atomic structure of edge terminations is shown to be critical, with zigzag edges contributing to plasmon broadening significantly more than armchair edges. This study demonstrates the ability of graphene nanostructures to host well-defined plasmons down to sizes below 10 nm, and it delineates a roadmap for understanding their main characteristics, including the role of finite size and nonlocality, thus providing a solid background for the emerging field of graphene nanoplasmonics.

KEYWORDS: plasmonics · graphene plasmons · nanophotonics · tight-binding · RPA response · graphene nanodisks · nanoribbons

to electrostatically control the frequency and even the mere existence of plasmon states. The electrostatic tunability of graphene plasmons has been recently demonstrated in measurements of the terahertz light absorption by ribbons¹⁸ and the infrared scattering strength of a tip situated near graphene.²³

* Address correspondence to
j.g.deabajo@csic.es.

Received for review December 7, 2011
and accepted January 4, 2012.

Published online January 04, 2012
10.1021/nn204780e

© 2012 American Chemical Society

The optical response of graphene has been extensively investigated on theoretical grounds in homogeneous^{15,20,24–26} and nanopatterned^{17,19,20,27,28} structures, although most of the reported work relies on a classical electromagnetic description of the carbon sheet, which is represented by a local, frequency-dependent conductivity. A first-principles analysis including non-local effects has only been performed for extended graphene^{15,24,25,29} and for plasmon energies in narrow (<1.5 nm) armchair ribbons.³⁰ The latter exhibit plasmons even when they are undoped, in contrast to zigzag ribbons,³⁰ thus indicating that carbon edge terminations play an important role in the band structure and the optical response of nanostructured graphene. Such a dramatic dependence on carbon edges is accompanied by opening of electron band gaps (~ 20 meV for a width of 25 nm) and formation of localized edge states in zigzag ribbons.^{30–34} Although these effects are expected to be small in samples with characteristic dimensions above 100 nm, a comprehensive study in truly nanometer-sized structures is still missing.

In this article, we present first-principles calculations of the optical response of graphene nanodisks and nanoribbons. We describe doped graphene using a tight-binding model for the electronic structure^{35,36} and the random-phase approximation (RPA)³⁷ for the dielectric response. The resulting plasmon energies are predicted to follow quite closely those obtained from classical electrodynamics, except for sizes below ~ 10 nm, for which the molecular character of the carbon structures shows up by splitting the plasmon features into an increasing number of resonances as the size is reduced. In contrast, the plasmon lifetime displays a slower convergence toward classical theory and remains well below the relaxation time of homogeneous graphene even in structures larger than 20 nm. Our results demonstrate that doped graphene is capable of sustaining plasmons down to sub-10 nm structures, whose understanding requires going beyond classical local electrodynamics.

RESULTS AND DISCUSSION

First-Principles Description of Graphene Plasmons. At low energies below ~ 1 eV, the optical response of carbon allotropes is dominated by excitations of the π valence band, formed by electrons residing in the carbon 2p orbitals oriented perpendicularly with respect to the local carbon bonds and populated on average with one electron per carbon site (*i.e.*, this band is half filled due to spin degeneracy). The σ band lies deeper in energy and only contributes with a nearly uniform background polarization. Excited states are formed when π electrons hop between neighboring sites, and thus, it is natural to study the π band within a tight-binding model, in which one-electron states are linear combinations of carbon 2p orbitals (one per site).³⁵ A tight-binding Hamiltonian is then defined as

explained in the Methods section. Despite its simplicity, the tight-binding model provides a reliable description of the electronic structure,³⁶ particularly when used inside the RPA susceptibility (see below), which is an integrated quantity that should be rather insensitive to corrections affecting individual electron levels due to many-body interactions^{38,39} and edge effects.⁴⁰ As a first step in our calculation, we diagonalize this Hamiltonian for patterned graphene and find its single-electron states. For finite structures formed by N atoms (*e.g.*, nanodisks), this leads to a set of N doubly spin-degenerate states. In neutral graphene, only half of them are occupied, but in doped graphene configurations, they are filled up to a Fermi energy (E_F) relative to undoped carbons sheets.

The structures under discussion are small compared to the light wavelength, and consequently, they are accurately described within the electrostatic limit, in which the charge density ρ_I induced on each carbon site I can be expressed in terms of the self-consistent potential ϕ_I acting at all sites I' as

$$\rho_I = \sum_{I'} \chi_{II'}^0 \phi_{I'} \quad (1)$$

where $\chi_{II'}^0$ is the noninteracting susceptibility. Furthermore, we obtain χ^0 using the RPA,³⁷ in which only electron–hole pair excitations are considered. The susceptibility is then constructed from the expansion coefficients $a_{jj'}$ of the tight-binding states $\sum_I a_{jj'I} |I\rangle$, where j is a state label and I runs over carbon sites. More precisely³⁷

$$\chi_{II'}^0(\omega) = \frac{2e^2}{\hbar} \sum_{jj'} (f_{j'} - f_j) \frac{a_{jj'} a_{jj'}^* a_{j'I}^* a_{j'I'}}{\omega - (\varepsilon_j - \varepsilon_{j'}) + i/2\tau} \quad (2)$$

where ω is the light frequency, $\hbar\varepsilon_j$ is the energy of state j and $f_j = \{\exp[\hbar\varepsilon_j - E_F]/k_B T] + 1\}^{-1}$ is its occupation at temperature T (we set $T = 300$ K throughout this work), τ is an intrinsic relaxation time,⁴¹ and the factor of 2 before the sum stems from spin degeneracy. A direct evaluation of χ^0 for a carbon cluster formed by N atoms (*e.g.*, $N \sim 12\,000$ for 20 nm disks) constitutes a *tour de force* that requires summing $\sim N^4$ terms, so instead, we employ an alternative procedure based upon the use of the fast Fourier transform (FFT), which reduces the task to $\sim N^3$ operations, as explained in the Methods section. Incidentally, the orthogonality of the electron states directly implies $\sum_I \chi_{II'}^0 = 0$, and this in turn guarantees the vanishing of the net induced charge $\sum_I \rho_I = 0$ (see eq 1). Now, the total potential is the sum of the external potential ϕ^{ext} and the potential produced by the induced charges:

$$\phi_I = \phi_I^{\text{ext}} + \sum_{I'} v_{II'} \rho_{I'} \quad (3)$$

where $v_{II'}$ is the Coulomb interaction produced on the p orbital at site I by a unit charge with the distribution of the p orbital at site I' . This interaction is roughly $1/r$ for $I \neq I'$, whereas $v_{II} = 0.58$ atomic units (au). Nonetheless, we calculate $v_{II'}$ rigorously using the probability distribution

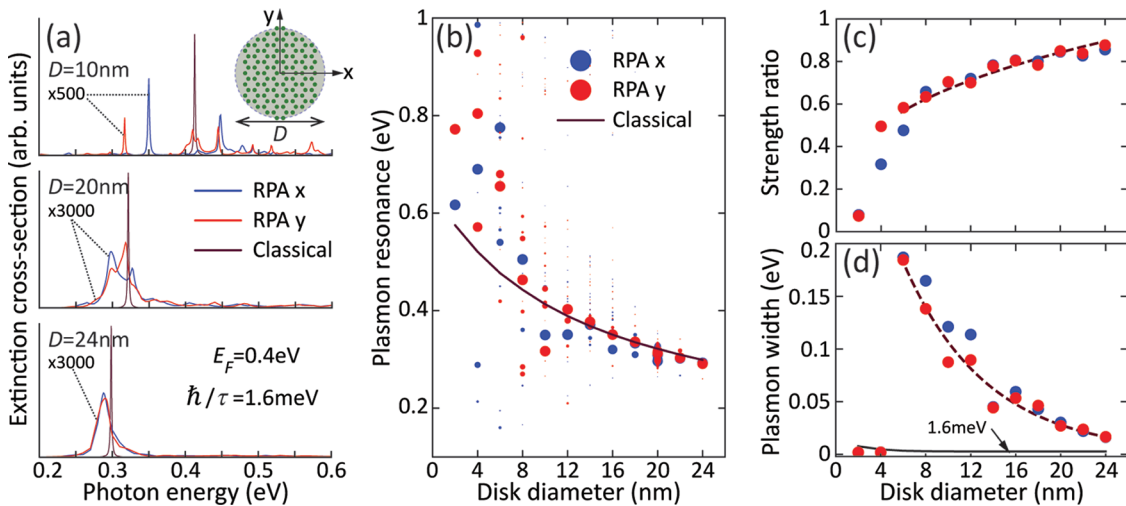


Figure 1. Plasmons in graphene nanodisks. (a) Extinction cross section calculated in the RPA for self-standing graphene disks of different size and for incidence perpendicular to the disks with polarizations along the x or y directions (see inset), compared with classical electromagnetic theory. The main features in the plot correspond to induced parallel dipoles. (b) Spectral features in the extinction spectra (symbols) compared with the classical electromagnetic dipole plasmon energy as a function of disk size. The symbol sizes are scaled with the strength of the spectral peaks. (c) Ratio of integrated area in the spectra calculated within the RPA to the classical plasmon peak area. (d) Plasmon half-area width in our RPA calculations (symbols) and in the classical theory (lower curve, which roughly coincides with the input width $\hbar\tau^{-1} = 1.6 \text{ meV}$). Dashed curves in (c) and (d) are guides to the eye. The Fermi energy is $E_F = 0.4 \text{ eV}$ in all cases.

associated with carbon 2p orbitals taken from tabulated atomic data.⁴² We self-consistently solve eqs 1 and 3 to find ρ_i and then compute the absorption cross section

$$\sigma^{\text{abs}} = 4\pi(\omega/c)\text{Im}\{\alpha(\omega)\}$$

from the polarizability α , which is in turn given by the dipole induced upon illumination with a uniform electric field \mathbf{E}^{ext} (*i.e.*, $\phi_i^{\text{ext}} = -x_i E^{\text{ext}}$) as

$$\alpha(\omega) = (1/E^{\text{ext}}) \sum_i x_i \rho_i$$

where x_i are the projections of the atomic coordinates along the external field direction.

Finite-Size and Nonlocal Effects in Graphene Nanodisks. We show in Figure 1a several examples of extinction spectra calculated for graphene nanodisks of different size and a common doping level ($E_F = 0.4 \text{ eV}$). A first striking observation is the presence of multiple peaks in the smallest disk under consideration (diameter $D = 10 \text{ nm}$). Rather than a proper clearly defined plasmon, the spectra for both orientations of the incident light polarization relative to the carbon lattice exhibit several narrow peaks, the width of which is roughly equal to the intrinsic width $\hbar\tau^{-1}$ introduced through eq 2. For larger structures ($D = 20$ and 24 nm), these peaks evolve toward a single prominent peak of larger width, rather independent of the orientation of the incident polarization. A similar trend toward a single plasmon peak is observed when increasing the intrinsic width (see Figure S6 in the Supporting Information). When compared with a classical calculation of the extinction (black curves), we see that this is in fact the dipolar plasmon sustained by these structures. The classical calculation is based upon a

description of the graphene in terms of a frequency-dependent local surface conductivity, which is then used to match the electromagnetic boundary conditions imposed by Maxwell's equations in the presence of the nanodisks (see Methods). Remarkably, the classically calculated plasmon exhibits a narrow width $\sim\hbar\tau^{-1}$, in contrast to the much broader plasmon features predicted by our first-principles RPA calculations.

Figure 1b presents a summary of nanodisk extinction spectra obtained as a function of disk diameter for polarizations either along x or y (see inset in Figure 1a). The actual spectra are given in the Supporting Information (Figure S8). For each value of the diameter, this plot contains several symbols indicating the different peaks that show up in the spectra. The size of each symbol is roughly proportional to the strength of the corresponding peak. We observe a clear trend of convergence of spectral features toward a single plasmon band as the diameter increases. Actually, convergence toward the plasmon energy predicted by the classical model is nearly achieved for diameters above $\sim 20 \text{ nm}$. For smaller sizes, the strength of the plasmon is generally situated at larger energies (*i.e.*, it is blue-shifted) compared to the classical calculation.

In order to quantify the plasmon width for small diameters, given the complex structure of the spectra, we introduce the half-area width, which we define as the accumulated width of a spectral region centered around the average plasmon energy and containing half of the integrated area under the spectrum (in particular, the half-area width is equal to the fwhm for single Lorentzian peaks). In practice, we define a

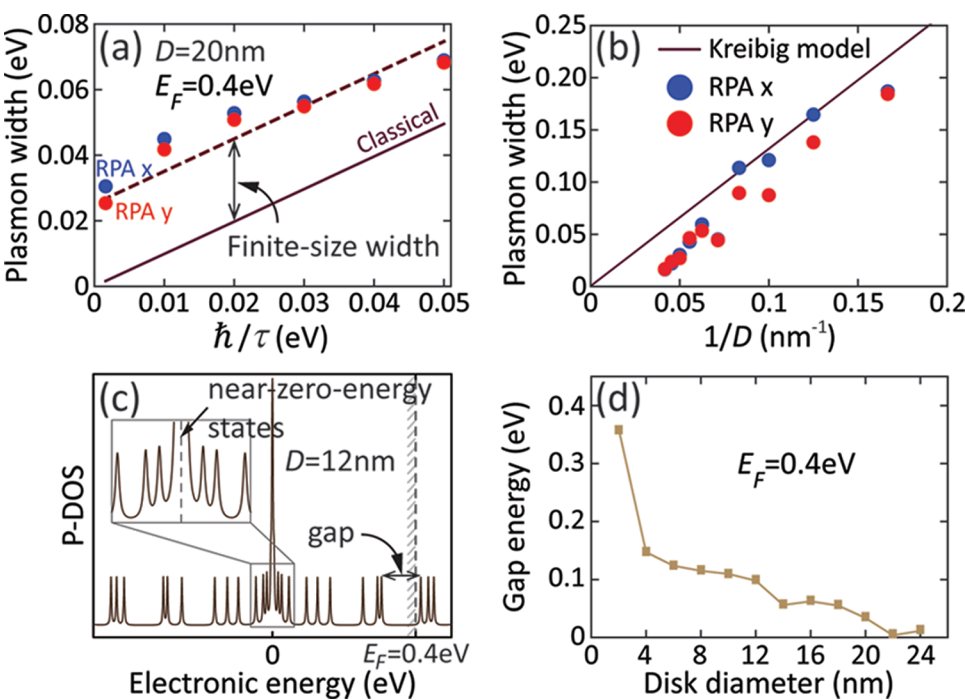


Figure 2. Finite-size and nonlocal effects in the plasmons of graphene nanodisks. (a) Evolution of the half-area dipole plasmon width as a function of input intrinsic width $\hbar\tau^{-1}$. A nearly constant difference between these two is found and denoted finite-size width. (b) Variation of the finite-size width with disk diameter D , showing a roughly linear dependence with $1/D$. The straight line corresponds to a plasmon width given by $2\hbar\nu_F/D$. (c) Pseudodensity of states (P-DOS) in a 12 nm disk, showing a gap near the Fermi energy $E_F = 0.4$ eV and near-zero-energy states. (d) Gap energy dependence on disk size.

spectral window in the 0–1 eV range for this purpose. A trend of convergence toward the classical result ($\sim\hbar\tau^{-1}$), similar to what happened with the plasmon energy, is observed for the plasmon width, although this is still well above the intrinsic damping $\hbar\tau^{-1}$ even for a relatively large diameter $D = 24$ nm (Figure 1d). (Incidentally, small disks of 2 nm in diameter only display one peak within the spectral window under consideration (see Supporting Information, Figure S8), the width of which roughly corresponds to the intrinsic damping. Larger disks contain several peaks, and this explains the sudden jump in plasmon width.) Likewise, the ratio of plasmon areas calculated from the RPA and from the classical model (Figure 1c, with the areas integrated over the noted spectral window) is slowly converging toward 1 with increasing diameter. It should be noted that the finite-size effects under discussion occur even for plasmon energies well below E_F (large diameters in Figure 1), and therefore, their origin is different from Landau damping taking place in homogeneous graphene when the plasmon band overlaps the electron–hole excitation region at plasmon energies roughly above the Fermi energy.

The additional finite-size width of the plasmon with respect to the intrinsic width $\hbar\tau^{-1}$ seems to be well preserved over a large range of τ (Figure 2a), thus indicating that it is consistently produced by finite-size and edge effects. It rapidly decreases with increasing disk diameter (Figure 2b), although it is still taking considerable values well above $\hbar\tau^{-1}$ for $D = 24$ nm. This

behavior can be ultimately understood by noticing the finite spectral separation between different individual excitations in small structures (see Figure 1a and Figure S8 in the Supporting Information), which, even after incorporating the interaction between excited electron–hole pairs in a self-consistent fashion through the RPA, continue to be separated by a considerable distance in photon energy. For finite relaxation time τ , these peaks coalesce into a single broader plasmon feature (see Figure S6 in the Supporting Information), thus transforming the energy distance between individual excitations into an effective broadening of the plasmon as a whole.

At this point, it is useful to examine the distribution of electronic energies. For example, a disk with $D = 12$ nm and $E_F = 0.4$ eV (Figure 2c) exhibits a characteristic electronic gap near the Fermi level that defines a minimum excitation energy and, therefore, also an optical gap. Moreover, it displays a pileup of electron states around zero energy, essentially localized near zigzag edges of the graphene nanodisk (see Figures S3 and S4 in the Supporting Information for more details). The complex interplay between electronic states *via* their mutual orthogonality enters this picture by producing more broadening (*i.e.*, larger energy separation between the constituent individual excitations noted above) when edge states are present (see also a related discussion for ribbons in next section). One might naively think that near-zero-energy edge states only contribute to broadening for plasmon energies

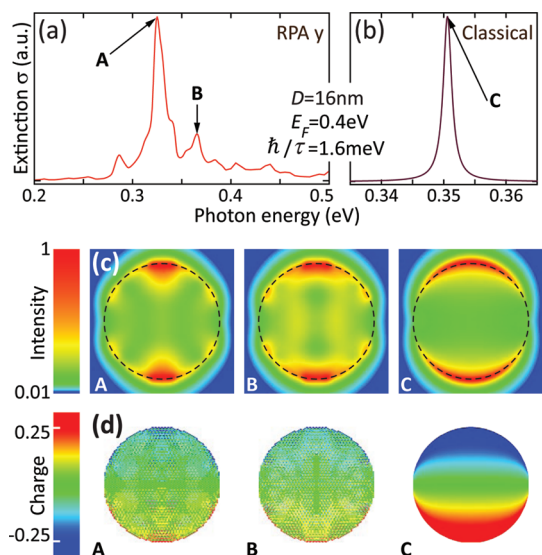


Figure 3. Fine structure in the plasmon features. (a,b) Extinction spectrum for a disk with physical parameters as shown by text insets, calculated within the RPA (a) and from a classical model (b). Light is incident normal to the disk with the electric field along the y direction. (c) Normalized electric field intensity (log scale) at a distance of 0.5 nm above the disk for features A and B of the RPA spectrum, compared to the classical calculation (C). The intensity enhancement relative to the incident field is 810, 64, and 2.7×10^5 in A–C, respectively. (d) Normalized charge-density amplitude (linear scale saturated outside $[-0.25, 0.25]$) for the same features as in (c).

exceeding the Fermi energy (see Figure 2c), but this is at odds with the smooth dependence of the plasmon width on disk size around the point where the plasmon energy is crossing E_F (*i.e.*, $D \approx 12$ nm; see Figure 1b,d). A possible mechanism of decoherence is related to the distortion of the electronic wave functions near zigzag edges, which is needed in order to fulfill the orthogonality of every electron state with respect to edge states. This distortion can potentially provide extra momentum needed to produce additional electron–hole pair transitions that couple to the plasmon, in contrast to the stringent momentum conservation conditions in homogeneous graphene. The electronic gap can also influence the plasmon width by limiting the number of available electron–hole transitions for a given plasmon energy. In this respect, it is interesting to note that the gap exhibits a similar trend as the finite-size width, with a strong decrease toward zero as the disk diameter increases.

The plasmon width shows a nearly linear dependence on $1/D$ (Figure 2b), similar to that of metallic nanoparticles.^{43,44} This is phenomenologically understood from Kreibig's model,⁴³ which associates the extra broadening with the time spanned between electron (or hole) edge collisions. The relevant electrons are moving at a speed close to the Fermi velocity v_F , and the increase in the plasmon decoherence rate for nanoparticles of diameter D is $\sim 2v_F/D$.⁴³ The straight line in Figure 2b corresponds to $2\hbar v_F/D$, in excellent agreement with the RPA width. This supports

the interpretation of the nanodisk plasmon width as originating in quantum confinement and finite-size effects, similar to what happens in metal nanoparticles. However, in contrast to nanoparticles, small disks of size below ~ 10 nm exhibit multiple excitations that emphasize the molecular character of these structures (see Supporting Information, Figure S8), possibly due to the low number of involved graphene electrons compared to metal nanoparticles of similar diameter. The role of edge states discussed above also introduces a clear difference with respect to nanoparticles.

The spectral structure of the plasmon is expected to be complex, as it results from accumulation of multiple peaks toward a single plasmon energy as the disk diameter increases. This is clearly illustrated in Figure 3, where a disk of size $D = 16$ nm is analyzed. The plasmon is not yet fully consisting of a single peak for the values of D and $\hbar\tau^{-1} = 1.6$ meV under consideration (Figure 3a). We show the near-field and the induced charge associated with two of the spectral features within the plasmon region, and we find very different spatial behavior (*cf.* A and B in Figure 3c,d), particularly when compared to the classical model (C). Additionally, the field enhancement obtained from the RPA is considerably smaller than that predicted by classical theory (see caption of Figure 3), in agreement with recent calculations for metallic dimers.⁴⁵ This information is important for assessing the strength of the interaction between this structure and additional elements such as molecules for potential use in biosensing or to achieve strong light–matter interaction.²⁰

Understanding Edge Effects in Nanoribbon Plasmons. An extension of the formalism presented above allows us to simulate graphene nanoribbons (see Methods). In particular, we consider ribbons with either zigzag or armchair edges exposed to a uniform electric field directed across the ribbon width, from which we calculate the absorption cross section under normal incidence conditions. The main results are summarized in Figure 4, which presents the evolution of the plasmon energy and the plasmon width for different edge terminations. Like in the nanodisks studied above, nanoribbon plasmons are dipolar and thus couple efficiently to external light. In contrast to disks, nanoribbons exhibit a single plasmon feature down to very small widths, presumably due to the fact that electron–hole transitions are summed over a continuum of electron parallel wave vectors along the ribbon direction (*i.e.*, the electronic spectrum is continuous in ribbons, but it is discrete in nanodisks). The plasmon energies obtained from first-principles calculations (Figure 4b, symbols) nicely converge toward the classical result for sizes above ~ 10 nm and show a small blue shift at small ribbon widths. The plasmon width also converges toward the intrinsic value determined by τ (Figure 4c), but this convergence is

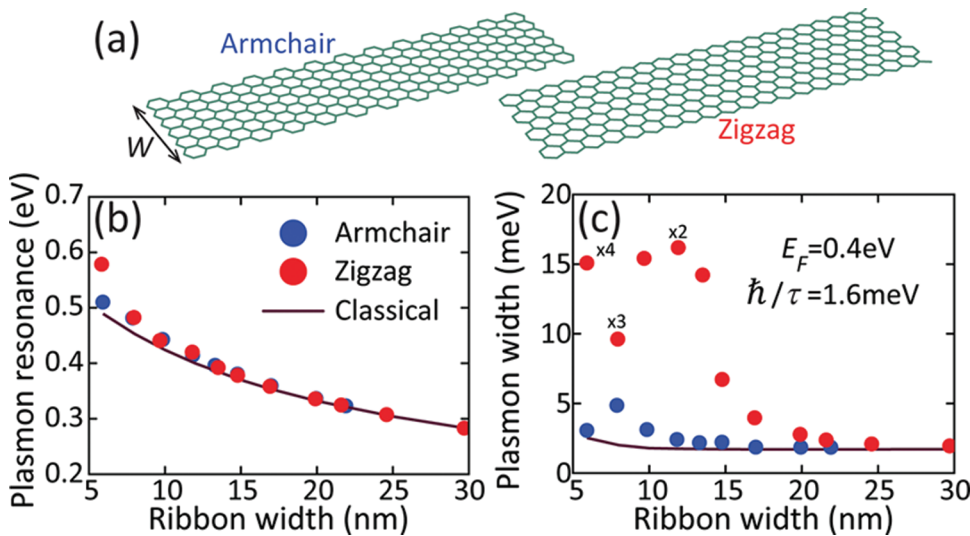


Figure 4. Plasmons in nanoribbons. (a) We consider nanoribbons with armchair and zigzag edges. The relative alignment between both edges is clearly shown in the figure. (b) Variation of the plasmon energy with ribbon width, calculated in the RPA (symbols) and from a classical electromagnetic description (curve). (c) Plasmon half-area width as a function of ribbon width.

remarkably faster in armchair ribbons. In contrast, zigzag ribbons host electron states confined to the edges,³¹ which seem to be responsible for the additional plasmon broadening.

Comparing ribbons and disks of similar size (width = diameter), the plasmon width in nanodisks is almost 1 order of magnitude larger than in zigzag ribbons (cf. Figure 1d and Figure 4c). This suggests that plasmon broadening in nanodisks and nanoribbons is due to different physical mechanisms. Quantum confinement can produce plasmon broadening because the plasmon finds new electron–hole pair excitations into which it can decay compared to homogeneous graphene; the finite size of the electron (hole) wave functions translates into extra momentum to fulfill energy-momentum conservation. This mechanism should be more efficient in nanodisks than in nanoribbons because disks have larger perimeter-to-area ratio. The inhomogeneous edges and edge-state distributions in nanodisks also contribute in a similar manner to broaden the plasmon, as explained above. These mechanisms are compatible with the large calculated broadening of nanodisk plasmons, exhibiting a nearly linear dependence on $1/D$ (Figure 2b). In contrast, the width of nanoribbon plasmons displays a more complicated dependence on the inverse ribbon width $1/W$ (see Supporting Information, Figure S10). We expect quantum confinement to be less effective in nanoribbons because the electron states are free to move along the spatial direction parallel to them. Edge states in zigzag ribbons are thus the likely origin of additional plasmon broadening in these structures, although their effect is diminished with respect to nanodisks because ribbons have uniform edges. These conclusions are further supported by the fact that armchair ribbons, in which edge states are not present,

display a much smaller plasmon broadening, comparable in magnitude to the classical calculation.

Edge states emerge with near-zero energy,³¹ so they contribute to the plasmon width for plasmon energies above E_F via excitation to unoccupied conduction states. This is what we observe in Figure 4: the plasmon energy exceeds the Fermi energy when the ribbon width drops below ~ 12 nm (Figure 4b), and the plasmon width rises enormously in narrower zigzag ribbons (Figure 4c). However, the width of zigzag ribbon plasmons is significantly larger than that of armchair ribbon plasmons up to a ribbon width of ≈ 20 nm, thus pointing to an additional mechanism other than direct excitation of edge states. A possible explanation is provided by the distinct band structures of armchair and zigzag ribbons, which allow transitions between states of opposite wave vector along the ribbon direction only in zigzag ribbons,³⁰ thus increasing the number of electron–hole decay channels available to the plasmons.

We have recently shown that for the ribbon widths W under consideration (\ll light wavelength) an electrostatic scaling law applies to the classically calculated plasmon frequency, namely²⁸

$$\eta = \frac{\text{Im}\{\sigma(\omega_p)\}}{\omega_p W} \quad (4)$$

where σ is the graphene surface conductivity and η is just a constant that only depends on the direction of light incidence and mode polarization. Under normal incidence conditions, the dipole plasmon frequency is obtained by setting $\eta = 0.0675$. Then, using the local RPA model for σ , as described in the Methods section, the solution of eq 4 yields a plasmon frequency that cannot be distinguished from the solid curve of

Figure 4b (full electrodynamic calculations) on the scale of the plot. Additionally, in the Drude model, the electrostatic scaling law predicts that the plasmon width equals the intrinsic width $\hbar\tau^{-1}$,²⁸ in good agreement with the solid curve of Figure 4c, except for ribbons of small width, <10 nm, for which the plasmon energy lies above E_F , thus being broadened by Landau damping, not accounted for by Drude. It is remarkable that this simple analytical law is in quantitative agreement with the RPA calculations here presented for the plasmon energy in ribbons wider than 10 nm and also for the plasmon width in armchair ribbons wider than ~10 nm and in zigzag ribbons wider than ~20 nm.

CONCLUSIONS

We have performed first-principles calculations of the optical response of doped graphene nanodisks and nanoribbons within the RPA using a tight-binding model for the electronic states. The plasmon width and frequency are dramatically influenced by nonlocal and quantum finite-size effects, compared to a classical electromagnetic description reported elsewhere.²⁰ Similar to what happens in small metallic nanoparticles,^{43–47} plasmon blue shifts are clearly observable due to these effects up to nanodisk diameters and ribbon widths above ~10 nm. Plasmon broadening is also significant up to sizes above ~25 nm compared to the plasmon width in homogeneous graphene. We attribute these effects to both the finite size of the structures and the presence of electronic edge states. In particular, localized electron states are supported by zigzag edges³¹ (see Supporting Information, Figures S3 and S4), which lead to extra plasmon broadening in ribbons with that kind of termination as compared to ribbons of similar size but with armchair edges instead. For small structures below ~20 nm, nanodisk plasmons display considerable fine structure that is clearly resolvable even when considering a conservative intrinsic broadening, thus emphasizing the molecular character of nanostructured graphene. This is in contrast to nanoribbons, which exhibit a single plasmon feature within the range of ribbon widths under consideration (5–30 nm). Actually, nanoribbons and nanoparticles share in common a large number of electronic states and optical transitions compared to nanodisks, which lead to a single plasmon feature rather than molecule-like modes at small sizes.

Plasmons in nanoribbons wider than 10 nm have been shown to rapidly converge in energy to the results predicted by classical electrodynamics, although the plasmon width is significantly affected by finite-size and edge effects in ribbons of widths below ~10 nm for armchair terminations and below ~20 nm in zigzag ribbons. Nanodisks contain a combination of these types of edge terminations, and thus, they are affected

by edge states, as well. Actually, the ratio of edge perimeter to graphene area is larger in nanodisks, which is consistent with the fact that plasmon blue shifts and broadenings occur in these structures up to large diameters compared to the ribbon widths. It must be noted that such small graphene structures have been recently synthesized,⁴⁸ therefore making the experimental verification of our work feasible in the short term, although it is still technically challenging to combine the required nanofabrication tools with good control over graphene doping and infrared optical measurements.

It is useful to realize that the number of electrons needed to dope a $D = 20$ nm graphene nanodisk up to a Fermi energy $E_F = 0.4$ eV is only $\approx (E_F D / 2\hbar v_F)^2 \approx 37$, where we use the electron density in doped homogeneous graphene ($n = E_F^2 / (\pi\hbar^2 v_F^2)$) for this estimate. Adding or removing one extra electron thus requires an attainable change of ≈ 5 meV in E_F , which results in a shift by ≈ 2 meV in plasmon energy, according to the electrostatic scaling law²⁸ ($\omega_p^2 D / E_F = \text{constant}$), although actual values might be influenced by the finiteness of the electronic gap. These numbers point to the unprecedented possibility of inducing observable plasmon shifts by electrically injecting one single electron to the graphene structure. Careful analysis of finite-size effects is required to analyze this phenomenon, which can find application to optical switching with ultrasmall amounts of electric energy.

In practical terms, nanodisk doping presents a technical challenge because of the damaging effects that conventional metallic leads can have on the optical response of the structure. Decorating the disks with bridges made of a transparent, conductive material can be a solution, whereas chemical doping is another option, which can be useful for achieving optical sensing of chemical changes in a fluid surrounding the graphene. Alternatively, local doping in a small graphene region of an extended flake can be driven by a nearby charged metal tip, so that the resulting structure mimics a nanodisk of diameter comparable to the tip–graphene separation. This configuration should allow plasmons to be confined in the doped region, possibly exhibiting increased plasmon lifetimes due to the absence of damaging edge states.

In summary, a classical electromagnetic treatment is a reasonable approximation only for graphene ribbons and disks with characteristic dimensions of at least several tens of nanometers, whereas a proper quantum description of the electronic states and their collective excitations as presented here is needed for smaller sizes. Our work is thus serving two purposes: (i) it provides a solid justification for the use of classical theory in large structures; and (ii) it presents a landscape for plasmons in smaller structures, which can find potential application to nanophotonic devices

(e.g., in plasmon–molecule interactions, ultrasensitive optical detection through SERS or SEIRA, and the noted variation of plasmon energy by adding or removing

one single electron to/from a graphene nanoisland), but require careful treatment of nonlocal and finite-size effects.

METHODS

Tight-Binding Model. In the tight-binding approach, the one-electron states j in the π band are constructed as linear combinations of carbon 2p orbitals $\sum a_{jl}|l\rangle$, where l runs over carbon sites. Incidentally, we disregard spin–orbit interactions, so that electron spin enters the RPA response just through an overall factor of 2 in the noninteracting susceptibility χ^0 (see eq 2). We assume orthogonality between site states, $\langle ll' \rangle = \delta_{ll'}$. The only nonzero elements of the tight-binding Hamiltonian H involve nearest neighbors l and l' , for which $\langle ll'Hll' \rangle = -t$, where the hopping energy t is a fitting parameter. In homogeneous graphene, this model predicts a band structure characterized by two inequivalent so-called Dirac cones, crossing the Fermi level at two inequivalent K corner points of the hexagonal first Brillouin zone with an energy dependence $\approx \pm \hbar v_F |k|$,^{35,49} where k is the electron wave vector relative to the corresponding Dirac point, $v_F \approx 3ta_0/2\hbar$ is the Fermi velocity, and $a_0 = 1.421$ Å is the C–C bond distance. The Dirac cone has been traced through photoemission measurements,⁵⁰ from which fine corrections to the band structure have been resolved, although we expect them to be washed out by summing over electron–hole pairs in χ^0 . The measured Fermi velocity $v_F \approx 10^6$ m/s leads to a hopping parameter $t \approx 3.1$ eV, which is close to the actual value that we use here ($t \approx 2.8$ eV), deduced from both STM measurements of graphene nanoislands⁴⁸ and fits to *ab initio* calculations.³⁶ Incidentally, we neglect next-nearest-neighbor hopping, which is believed to contribute to H with terms ~ 0.1 eV.⁵¹ Furthermore, we are treating carbon edges with the same hopping parameter and perfect hexagonal structure as atoms in homogeneous graphene, while a more proper description leads to reconstruction and modified electronic wave functions,⁵² but summation over states in χ^0 should minimize this type of effect. In this respect, first-principles calculations beyond the tight-binding model have been reported for nanoribbons,^{53,54} from which no significant corrections are expected to emerge in the optical response.

Evaluation of the RPA Susceptibility in N^3 Time Using the Fast Fourier Transform. Direct summation of eq 2 involves $\sim N^4$ operations. This task becomes currently unaffordable for the size of the structures considered in this work. Instead, we evaluate χ^0 in N^3 time by writing^{55,56}

$$\chi_{ll'}^0(\omega) = \frac{2e^2}{\hbar} \int \frac{S_{ll'}(\omega')d\omega'}{\omega - \omega' + i/2\tau} \quad (5)$$

where

$$\begin{aligned} S_{ll'}(\omega) &= \sum_{jj'} (f_j - f_j) a_{jl} a_{jl}^* a_{j'l}^* a_{j'l} \delta[\omega - (\varepsilon_j - \varepsilon_{j'})] \\ &= \int d\omega' [F_{ll'}(\omega')G_{ll'}^*(\omega' - \omega) - G_{ll'}(\omega')F_{ll'}^*(\omega' - \omega)] \end{aligned} \quad (6)$$

is a spectral function and

$$\begin{bmatrix} F_{ll'}(\omega) \\ G_{ll'}(\omega) \end{bmatrix} = \sum_j a_{jl} a_{jl}^* \delta(\omega - \varepsilon_j) \begin{bmatrix} 1 - f_j \\ f_j \end{bmatrix} \quad (7)$$

are auxiliary functions, the evaluation of which takes a time proportional to N^3 (see below). The integral of eq 6 is then carried out using the FFT. Details on the convergence of this method are

provided in the Supporting Information (Figure S5). Incidentally, according to eqs 1 and 3, the self-consistent potential acting on the carbon atoms reduces to $\phi = (1 - \mathbf{v} \cdot \boldsymbol{\chi}^0)^{-1} \cdot \boldsymbol{\phi}^{\text{ext}}$, where the dot indicates matrix multiplication and the atomic-site label l is used as the matrix index. The matrix inversion needed to evaluate ϕ also takes a time $\sim N^3$.

The electron energies are limited to a finite range $\hbar|\varepsilon_j| < \hbar\omega_{\max}$ and therefore, we only need to compute the auxiliary functions $F_{ll'}(\omega)$ and $G_{ll'}(\omega)$ for ω within that range, over which we define a finite grid of N_ω frequencies ω_n . In order to facilitate the convolution discussed below, we take equally spaced frequencies, and N_ω is chosen to be a power of 2. We evaluate the auxiliary functions by splitting the weight of the δ functions in eq 7 into neighboring frequencies, so that each term j contributes to $F_{ll'}(\omega_n)$ as⁵⁵ $a_{jl} a_{jl}^* (1 - f_j)(\varepsilon_j - \omega_n)/(\omega_{n+1} - \omega_n)$ and to $F_{ll'}(\omega_{n+1})$ as $a_{jl} a_{jl}^* (1 - f_j)(\omega_{n+1} - \varepsilon_j)/(\omega_{n+1} - \omega_n)$, and likewise for G , with ε_j lying between ω_n and ω_{n+1} . This procedure has to be repeated over the N^2 combinations of sites l and l' for each of the N states j , so that it takes a time $\sim N^3$, with independence of the number of frequencies N_ω .

We evaluate the convolution of eq 6 using the FFT in a time roughly proportional to $N \log_2 N_\omega$ for each combination of l and l' , thus preserving the approximate N^3 time scaling of the overall computation. This yields $S_{ll'}(\omega_n)$ over a frequency grid spanning the range $|\omega_n| < 2\omega_{\max}$. The FFT is actually carried out using the FFTW package.⁵⁷

Finally, the integral of eq 5 is calculated from S by performing the frequency integral over each element of the ω grid:

$$\chi_{ll'}^0(\omega) \approx \sum_n W_n S_{ll'}(\omega_n)$$

where the weights

$$W_n = \frac{4e^2}{\hbar} \left[\int_{\omega_n}^{\omega_{n+1}} \frac{\omega' d\omega'}{(\omega + i/2\tau)^2 - \omega'^2} \left(\frac{\omega_{n+1} - \omega'}{\omega_{n+1} - \omega_n} \right) \right. \\ \left. + \int_{\omega_{n-1}}^{\omega_n} \frac{\omega' d\omega'}{(\omega + i/2\tau)^2 - \omega'^2} \left(\frac{\omega' - \omega_{n-1}}{\omega_n - \omega_{n-1}} \right) \right] \quad (8)$$

are analytically computed once and for all the first time that they are needed.

RPA for Nanoribbons. We consider nanoribbons of period b along their direction of translational symmetry, containing N carbon atoms in the unit cell. We describe electronic states of ribbons with zigzag and armchair edges within the tight-binding model, which faithfully follows the ribbon electronic structures previously reported in the literature.³¹ More precisely, we use Bloch's theorem⁵⁸ to construct a complete set of electron eigenstates labeled by both the carbon site index l within the first unit cell and the Bloch wave vector k spanning the first Brillouin zone ($|kb| < \pi$). The eigenstate amplitudes thus become $a_{jl,k} e^{ikbn}$, where the integer n runs over unit cells. It is convenient to decompose the externally applied field in terms of its Fourier components along the ribbon direction z , on which they depend as $\phi_{l,q}^{\text{ext}} e^{iqz}$. After some algebra, we find that the induced charge density and the potential depend on n through a factor e^{iqbn} ; the total potential reads

$$\phi_{l,q} = \phi_{l,q}^{\text{ext}} + \sum_l V_{ll',q} \rho_{l',q}$$

where

$$V_{ll',q} = \sum_n V_{l0,l'n} e^{iqbn}$$

involves a sum of the Coulomb interaction $V_{l0,l'n}$ between atoms l and l' separated by n unit cells (charge neutrality, leading to

$\Sigma \chi_{IIr,q}^0 = 0$, allows us to subtract $1/|nb|$, from $n \neq 0$ terms in this sum to accelerate its convergence); the induced density becomes $\rho_{l,q} = \Sigma_l \chi_{IIr,q}^0 \phi_{l,q}$; and the noninteracting RPA susceptibility appropriate for the 1D translational symmetry reads

$$\begin{aligned} \chi_{IIr,q}^0(\omega) &= \sum_n \chi_{10,r,n} e^{iqbn} \\ &\approx \frac{2e^2}{\hbar} \frac{b}{2\pi} \int_{-\pi/b}^{\pi/b} dk \sum_{jj'} (f_{j',k-q} - f_{j,k}) \frac{a_{j,l,k} a_{j',l,k-q}^*}{\omega - (\varepsilon_{j,k} - \varepsilon_{j',k-q}) + i/2\tau} \end{aligned}$$

where we have approximated $qb \ll 1$. We compute $\chi_{IIr,q}^0$ by performing the k integral using N_k equally spaced points. In practice, we use $N_k \sim 10^4$ to achieve convergence in the spectra for $\hbar\tau^{-1} \sim 2$ meV. We apply this formalism to a uniform electric field E^{ext} oriented along the ribbon width (*i.e.*, an external potential $-x_I E^{\text{ext}}$ with $q = 0$, where x_I is the coordinate of atom I along the graphene direction normal to z). Finally, the absorption cross section reduces to

$$\sigma = \frac{4\pi\omega L}{c} \sum_I x_I \text{Im} \left\{ \frac{\rho_{I,q=0}}{E^{\text{ext}}} \right\}$$

where L is the ribbon length.

Intrinsic Relaxation Time. In practice, τ in eq 2 represents an intrinsic relaxation time produced by inelastic electron–electron, electron–phonon, and electron–impurity scattering. Actually, electron–phonon coupling plays a leading role at plasmon energies above the in-plane optical phonon energy ~ 0.2 eV.^{15,34} A first-principles treatment of the relaxation time must involve many-body interactions, whose computation is outside the scope of the present work and becomes extremely challenging even for homogeneous graphene.^{38,39} Here, unless otherwise stated, we take the empirical value $\tau = 10^{-12} E_F$ in seconds, where E_F is expressed in eV, as estimated from a measured dc mobility of $10\,000 \text{ cm}^2/(\text{V}\cdot\text{s})$.^{15,59,60} This renders τ large compared to the relaxation produced by finite-size and edge effects in the nanostructures under discussion, and therefore, the conclusions of our work are rather independent of the exact choice of τ .

Classical Electromagnetic Calculations. We compare our RPA results with classical electromagnetic theory throughout this paper. Classical theory is computed here by rigorously solving the Maxwell equations using the boundary element method (BEM)^{20,61} for nanodisks and nanoribbons. In the BEM, graphene is modeled as a thin film of edges rounded by semicircular profiles and characterized by a dielectric function $1 + 4\pi t\sigma/\omega t$, where t is the film thickness and $\sigma(\omega)$ is the frequency-dependent surface conductivity. We use $t = 0.1$ nm, which is well converged with respect to the $t \rightarrow 0$ limit (see Supporting Information, Figures S12 and S13). Most importantly, we take $\sigma(\omega)$ from the local limit of the random-phase approximation for extended graphene (*i.e.*, for zero parallel wave vector), which is available in analytical form in the literature^{24,25} and reproduced in the Supporting Information for convenience. By construction, this classical approach must exactly converge to our RPA calculations in the limit of large disk radius or ribbon width for vanishing parallel wave vector. However, dramatic deviations between the RPA and the classical local theory are reported in this work for disks (ribbons) of finite radius (width), which are shown to decrease with increasing disk (ribbon) size beyond a few tens of nanometers.

Acknowledgment. We thank F. Guinea, F.H.L. Koppens, and D. Sánchez-Portal for helpful and enjoyable discussions. This work has been supported in part by the Spanish MICINN (MAT2010-14885 and Consolider NanoLight.es) and the European Commission (FP7-ICT-2009-4-248909-LIMA and FP7-ICT-2009-4-248855-N4E). A.M. acknowledges financial support through FPU from the Spanish ME.

Supporting Information Available: We provide additional information on the construction of carbon atom clusters for tight-binding calculations, one-electron states, electron edge states, convergence of the FFT method for the evaluation of χ^0 , dependence of calculated absorption spectra on the relaxation time τ , sensitivity of those spectra to edge terminations, cluster size dependence of absorption, plasmon-peak structure, the local RPA conductivity of homogeneous graphene, and convergence of electromagnetic calculations with graphene

thickness. This material is available free of charge via the Internet at <http://pubs.acs.org>.

REFERENCES AND NOTES

- Xu, H.; Bjerneld, E. J.; Käll, M.; Börjesson, L. Spectroscopy of Single Hemoglobin Molecules by Surface Enhanced Raman Scattering. *Phys. Rev. Lett.* **1999**, *83*, 4357–4360.
- Talley, C. E.; Jackson, J. B.; Oubre, C.; Grady, N. K.; Hollars, C. W.; Lane, S. M.; Huser, T. R.; Nordlander, P.; Halas, N. J. Surface-Enhanced Raman Scattering from Individual Au Nanoparticles and Nanoparticle Dimer Substrates. *Nano Lett.* **2005**, *5*, 1569–1574.
- Álvarez-Puebla, R. A.; Liz-Marzán, L. M.; García de Abajo, F. J. Light Concentration at the Nanometer Scale. *J. Phys. Chem. Lett.* **2010**, *1*, 2428–2434.
- O'Neal, D. P.; Hirsch, L. R.; Halas, N. J.; Payne, J. D.; West, J. L. Photo-Thermal Tumor Ablation in Mice Using Near Infrared-Absorbing Nanoparticles. *Cancer Lett.* **2004**, *209*, 171–176.
- Loo, C.; Lowery, A.; Halas, N. J.; West, J. L.; Drezek, R. Inmunotargeted Nanoshells for Integrated Cancer Imaging and Therapy. *Nano Lett.* **2005**, *5*, 709–711.
- Knight, M. W.; Sobhani, H.; Nordlander, P.; Halas, N. J. Photodetection with Active Optical Antennas. *Science* **2011**, *332*, 702–704.
- Catchpole, K. R.; Polman, A. Plasmonic Solar Cells. *Opt. Express* **2008**, *16*, 21793–21800.
- Atwater, H. A.; Polman, A. Plasmonics for Improved Photovoltaic Devices. *Nat. Mater.* **2010**, *9*, 205–213.
- Zia, R.; Schuller, J. A.; Chandran, A.; Brongersma, M. L. Plasmonics: The Next Chip-Scale Technology. *Mater. Today* **2006**, *9*, 20–27.
- Danckwerts, M.; Novotny, L. Optical Frequency Mixing at Coupled Gold Nanoparticles. *Phys. Rev. Lett.* **2007**, *98*, 026104.
- Harutyunyan, H.; Palomba, S.; Renger, J.; Quidant, R.; Novotny, L. Nonlinear Dark-Field Microscopy. *Nano Lett.* **2010**, *10*, 5076–5079.
- Chang, D. E.; Sørensen, A. S.; Demler, E. A.; Lukin, M. D. A Single-Photon Transistor Using Nanoscale Surface Plasmons. *Nat. Phys.* **2007**, *3*, 807–812.
- Manjavacas, A.; García de Abajo, F. J.; Nordlander, P. N. Quantum Plexcitonics: Strongly Interacting Plasmons and Excitons. *Nano Lett.* **2011**, *11*, 2318–2323.
- Novotny, L.; Hecht, B. *Principles of Nano-Optics*; Cambridge University Press: New York, 2006.
- Jablan, M.; Buljan, H.; Soljačić, M. Plasmonics in Graphene at Infrared Frequencies. *Phys. Rev. B* **2009**, *80*, 245435.
- Papasimakis, N.; Luo, Z.; Shen, Z. X.; De Angelis, F.; Di Fabrizio, E.; Nikolaenko, A. E.; Zheludev, N. I. Graphene in a Photonic Metamaterial. *Opt. Express* **2010**, *18*, 8353–8359.
- Vakil, A.; Engheta, N. Transformation Optics Using Graphene. *Science* **2011**, *332*, 1291–1294.
- Ju, L.; Geng, B.; Horng, J.; Girit, C.; Martin, M.; Hao, Z.; Bechtel, H. A.; Liang, X.; Zettl, A.; Shen, Y. R.; et al. Graphene Plasmonics for Tunable Terahertz Metamaterials. *Nat. Nanotechnol.* **2011**, *6*, 630–634.
- Thongrattanasiri, S.; Koppens, F. H. L.; García de Abajo, F. J. Total Light Absorption in Graphene; arXiv:1106.4460v1.
- Koppens, F. H. L.; Chang, D. E.; García de Abajo, F. J. Graphene Plasmonics: A Platform for Strong Light–Matter Interactions. *Nano Lett.* **2011**, *11*, 3370–3377.
- Efetov, D. K.; Kim, P. Controlling Electron–Phonon Interactions in Graphene at Ultrahigh Carrier Densities. *Phys. Rev. Lett.* **2010**, *105*, 256805.
- Chen, C. F.; Park, C. H.; Boudouris, B. W.; Horng, J.; Geng, B.; Girit, C.; Zettl, A.; Crommie, M. F.; Segalman, R. A.; Louie, S. G.; et al. Controlling Inelastic Light Scattering Quantum Pathways in Graphene. *Nature* **2011**, *471*, 617–620.
- Fei, Z.; Andreev, G. O.; Bao, W.; Zhang, L. M.; McLeod, A. S.; Wang, C.; Stewart, M. K.; Zhao, Z.; Dominguez, G.; Thiemens, M.; et al. Infrared Nanoscopy of Dirac Plasmons at the Graphene–SiO₂ Interface. *Nano Lett.* **2011**, *11*, 4701–4705.

24. Wunsch, B.; Stauber, T.; Sols, F.; Guinea, F. Dynamical Polarization of Graphene at Finite Doping. *New J. Phys.* **2006**, *8*, 318.
25. Hwang, E. H.; Das Sarma, S. Dielectric Function, Screening, and Plasmons in Two-Dimensional Graphene. *Phys. Rev. B* **2007**, *75*, 205418.
26. Nikitin, A. Y.; Guinea, F.; García-Vidal, F. J.; Martín-Moreno, L. Fields Radiated by a Nanoemitter in a Graphene Sheet. *Phys. Rev. B* **2011**, *84*, 195446.
27. Nikitin, A. Y.; Guinea, F.; García-Vidal, F. J.; Martín-Moreno, L. Edge and Waveguide Terahertz Surface Plasmon Modes in Graphene Microribbons. *Phys. Rev. B* **2011**, *84*, 161407(R).
28. Christensen, J.; Manjavacas, A.; Thongrattanasiri, S.; Koppens, F. H. L.; García de Abajo, F. J. Graphene Plasmon Waveguiding and Hybridization in Individual and Paired Nanoribbons. *ACS Nano* **2011**, DOI: 10.1021/nn2037626.
29. Yan, J.; Thygesen, K. S.; Jacobsen, K. W. Nonlocal Screening of Plasmons in Graphene by Semiconducting and Metallic Substrates: First-Principles Calculations. *Phys. Rev. Lett.* **2011**, *106*, 146803.
30. Brey, L.; Fertig, H. A. Elementary Electronic Excitations in Graphene Nanoribbons. *Phys. Rev. B* **2007**, *75*, 125434.
31. Brey, L.; Fertig, H. A. Electronic States of Graphene Nanoribbons Studied with the Dirac Equation. *Phys. Rev. B* **2006**, *73*, 235411.
32. Son, Y. W.; Cohen, M. L.; Louie, S. G. Energy Gaps in Graphene Nanoribbons. *Phys. Rev. Lett.* **2006**, *97*, 216803.
33. Han, M. Y.; Özylmaz, B.; Zhang, Y.; Kim, P. Energy Band-Gap Engineering of Graphene Nanoribbon. *Phys. Rev. Lett.* **2007**, *98*, 206805.
34. Beams, R.; Cancado, L. G.; Novotny, L. Low Temperature Raman Study of the Electron Coherence Length near Graphene Edges. *Nano Lett.* **2011**, *11*, 1177–1181.
35. Wallace, P. R. The Band Theory of Graphite. *Phys. Rev.* **1947**, *71*, 622–634.
36. Reich, S.; Maultzsch, J.; Thomsen, C.; Ordejón, P. Tight-Binding Description of Graphene. *Phys. Rev. B* **2002**, *66*, 035412.
37. Pines, D.; Nozières, P. *The Theory of Quantum Liquids*; W.A. Benjamin, Inc.: New York, 1966.
38. Trevisanutto, P. E.; Giorgetti, C.; Reining, L.; Ladisa, M.; Olevano, V. *Ab Initio* GW Many-Body Effects in Graphene. *Phys. Rev. Lett.* **2008**, *101*, 226405.
39. Park, C. H.; Giustino, F.; Spataru, C. D.; Cohen, M. L.; Louie, S. G. First-Principles Study of Electron Linewidths in Graphene. *Phys. Rev. Lett.* **2009**, *102*, 076803.
40. Wimmer, M.; Akhmerov, A. R.; Guinea, F. Robustness of Edge States in Graphene Quantum Dots. *Phys. Rev. B* **2010**, *82*, 045409.
41. The RPA response depends on ω through $(\omega + i/2\tau)^2 \approx \omega(\omega + i/\tau)$ (see eq 8). We introduce the factor of $1/2$ in $\omega + i/2\tau$ (e.g., in eq 2) in order to mimic the $\omega(\omega + i/\tau)$ dependence of the Drude model, which is consistent with electron-number conservation, as demonstrated in Mermin, N. D. Lindhard Dielectric Function in the Relaxation-Time Approximation. *Phys. Rev. B* **1970**, *1*, 2362–2363. This approximation is justified by the large values of τ under consideration.
42. Clementi, E.; Roetti, C. Roothaan-Hartree-Fock Atomic Wavefunctions. *At. Data Nucl. Data Tables* **1974**, *14*, 177–478.
43. Kreibig, U.; Genzel, L. Optical Absorption of Small Metallic Particles. *Surf. Sci.* **1985**, *156*, 678–700.
44. Halperin, W. P. Quantum Size Effects in Metal Particles. *Rev. Mod. Phys.* **1986**, *58*, 533–606.
45. Zuloaga, J.; Prodan, E.; Nordlander, P. Quantum Description of the Plasmon Resonances of a Nanoparticle Dimer. *Nano Lett.* **2009**, *9*, 887–891.
46. Kreibig, U.; Vollmer, M. *Optical Properties of Metal Clusters*; Springer-Verlag: Berlin, 1995.
47. García de Abajo, F. J. Nonlocal Effects in the Plasmons of Strongly Interacting Nanoparticles, Dimers, and Waveguides. *J. Phys. Chem. C* **2008**, *112*, 17983–17987.
48. Phark, S.; Borme, J.; Vanegas, A. L.; Corbetta, M.; Sander, D.; Kirschner, J. Direct Observation of Electron Confinement in Epitaxial Graphene Nanoislands. *ACS Nano* **2011**, *5*, 8162–8166.
49. Castro Neto, A. H.; Guinea, F.; Peres, N. M. R.; Novoselov, K. S.; Geim, A. K. The Electronic Properties of Graphene. *Rev. Mod. Phys.* **2009**, *81*, 109–162.
50. Bostwick, A.; Ohta, T.; Seyller, T.; Horn, K.; Rotenberg, E. Quasiparticle Dynamics in Graphene. *Nat. Photonics* **2007**, *3*, 36–40.
51. Deacon, R. S.; Chuang, K. C.; Nicholas, R. J.; Novoselov, K. S.; Geim, A. K. Cyclotron Resonance Study of the Electron and Hole Velocity in Graphene Monolayers. *Phys. Rev. B* **2007**, *76*, 081406(R).
52. van Ostaay, J. A. M.; Akhmerov, A. R.; Beenakker, C. W. J.; Wimmer, M. Dirac Boundary Condition at the Reconstructed Zigzag Edge of Graphene. *Phys. Rev. B* **2011**, *84*, 195434.
53. Prezzi, D.; Varsano, D.; Ruini, A.; Marini, A.; Molinari, E. Optical Properties of Graphene Nanoribbons: The Role of Many-Body Effects. *Phys. Rev. B* **2008**, *77*, 041404(R).
54. Agapito, L. A.; Cheng, H. P. *Ab Initio* Calculation of a Graphene-Ribbon-Based Molecular Switch. *J. Phys. Chem. C* **2007**, *111*, 14266–14273.
55. Shishkin, M.; Kresse, G. Implementation and Performance of the Frequency-Dependent GW Method within the PAW Framework. *Phys. Rev. B* **2006**, *74*, 035101.
56. Foerster, D.; Koval, P.; Sánchez-Portal, D. An $O(N^3)$ Implementation of Hedin's GW Approximation for Molecules. *J. Chem. Phys.* **2011**, *135*, 074105.
57. Frigo, M.; Johnson, S. G. The Design and Implementation of FFTW3. *Proc. IEEE* **2005**, *93*, 216–231.
58. Ashcroft, N. W.; Mermin, N. D. *Solid State Physics*; Harcourt College Publishers: New York, 1976.
59. Novoselov, K. S.; Geim, A. K.; Morozov, S. V.; Jiang, D.; Zhang, Y.; Dubonos, S. V.; Grigorieva, I. V.; Firsov, A. A. Electric Field Effect in Atomically Thin Carbon Films. *Science* **2004**, *306*, 666–669.
60. Novoselov, K. S.; Geim, A. K.; Morozov, S. V.; Jiang, D.; Katsnelson, M. I.; Grigorieva, I. V.; Dubonos, S. V.; Firsov, A. A. Two-Dimensional Gas of Massless Dirac Fermions in Graphene. *Nature* **2005**, *438*, 197–200.
61. García de Abajo, F. J.; Howie, A. Retarded Field Calculation of Electron Energy Loss in Inhomogeneous Dielectrics. *Phys. Rev. B* **2002**, *65*, 115418.

Supporting information for: Quantum Finite-Size Effects in Graphene Plasmons

Sukosin Thongrattanasiri, Alejandro Manjavacas, and F. Javier García de Abajo*

IQFR - CSIC, Serrano 119, 28006 Madrid, Spain

E-mail: J.G.deAbajo@csic.es

Construction of carbon atom clusters

As a first step in our calculations, we construct a cluster of atomic coordinates made of all N carbon atoms that lie inside a given geometrical shape. In particular, disks are parametrized by a circle of the required nominal diameter D , with its origin at the center of a C-C bond oriented along the x axis (see Figure S1). Obviously, edge atoms connected by dangling bonds are eliminated from the resulting cluster.

One-electron states

It is useful to examine some characteristic wave functions of graphene nanostructures. One-electron states are obtained by defining a tight-binding Hamiltonian matrix $H_{ll'}$ with indices l and l' running over atom sites, in which the only nonzero elements correspond to nearest neighbors and take the value $t = 2.8 \text{ eV}$.¹⁻⁴ Second nearest neighbors can be easily incorporated into this Hamiltonian with no additional computational cost, although we do not include this interaction here.

*To whom correspondence should be addressed

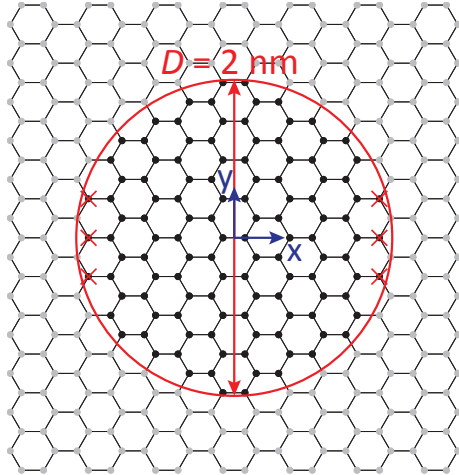


Figure S1: *Construction of a carbon atom cluster representing a graphene disk of nominal diameter D .* We start from an infinite graphene lattice oriented as shown in the figure. Only atoms contained within a circumference of diameter D are included in the cluster ($D = 2\text{ nm}$ in this example). The circumference is centered at a C-C bond. Edge carbon atoms with single bonds are eliminated (red-crossed atoms).

The N real eigenvalues and eigenvectors of the real, symmetric matrix H are obtained using standard numerical linear algebra.⁵ By construction, N states (including spin degeneracy) are obtained having negative energy, so that the Fermi energy of neutral graphene with one valence electron per carbon atom is $E_F = 0$. Doped graphene is thus characterized by the value of E_F relative to neutral graphene. Electron spin-orbit interaction is ignored in this tight-binding approach. Each tight-binding orbital is then populated by two electrons of opposite spin. The spin degree of freedom emerges in the calculation of the random-phase approximation (RPA) response just through a trivial factor of 2 in the non-interacting susceptibility χ^0 (see main paper).

Figure S2 shows the spatial variation of the electron wave function coefficients a_{jl} running over the carbon sites l of graphene disks of radii $D = 6\text{ nm}$ and $D = 20\text{ nm}$ for wave functions of different energy (upper row). Near-zero-energy (NZE) states (the energy is referred to the Fermi level of neutral graphene) are mostly concentrated near the edges, whereas states away from that region show characteristic standing wave patterns. These differences are also reflected in their spatial Fourier transforms. In particular, states away from the NZE region exhibit maxima centered at the K points (hexagon corners) of the first Brillouin zone of extended graphene. These maxima

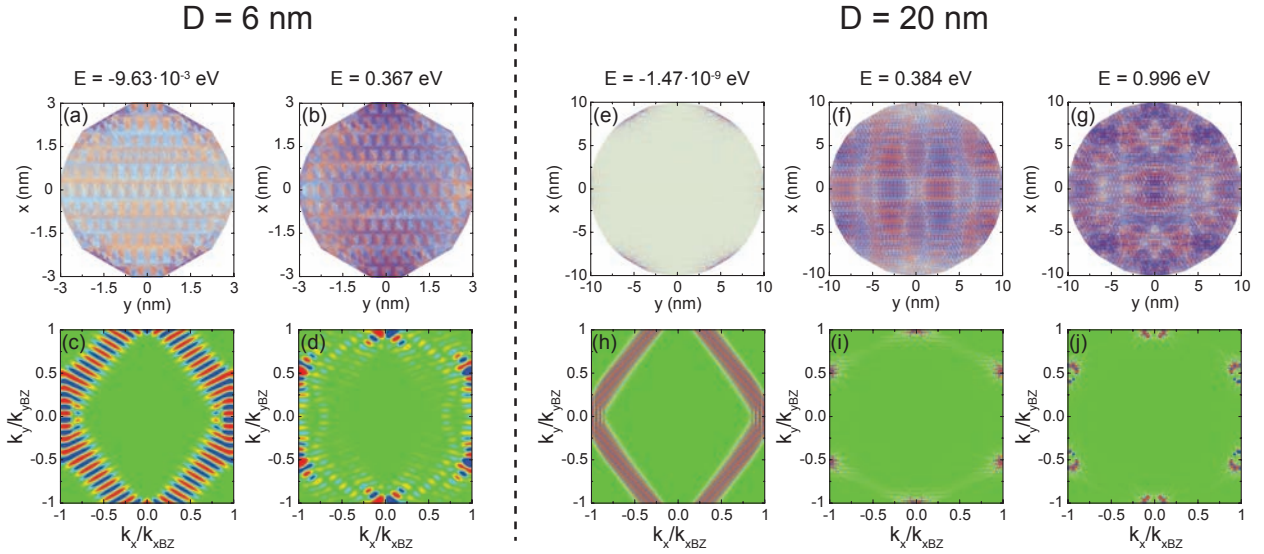


Figure S2: *Tight-binding electron states of graphene disks with two different diameters D and various energies with respect to the Fermi energy of neutral graphene.* **Upper row:** Spatial variation of several wave functions j of different energy $E \equiv \varepsilon_j$, defined by the real coefficients a_{jl} running over carbon sites l . **Lower row:** Spatial Fourier transform of the wave functions under consideration for wave vectors within the rectangle $|k_x| \leq k_{xBZ} = 2\pi/3a_0$ and $|k_y| \leq k_{yBZ} = 4\pi/3\sqrt{3}a_0$, where $a_0 = 1.421$ is the C-C bond length.

are more tightly focused at the K points for larger diameter. Interestingly, the Dirac cone structure of graphene emerges in the ring-like shape of the $D = 20\text{ nm}$ features when the energy reaches a sufficiently high value along the linear dispersion relation of the carbon sheet (see Figure S2j).

Electron edge states

The intriguing properties of NZE states are further explored in Figure S3 for a disk of diameter $D = 20\text{ nm}$. There is a clear pileup of states in the NZE region (Figure S3a), the average probability density of which mainly accumulates near the disk edges (Figure S3b, left), in contrast to other states of higher energy (Figure S3b, right). This is further illustrated by the probability density averaged over azimuthal angles, which is shown in Figure S3c as a function of state energy and radial distance to the disk center. Most states are distributed over the disk area, but NZE states display much higher probability near the edges (Figure S3d). It should be noted that edge states

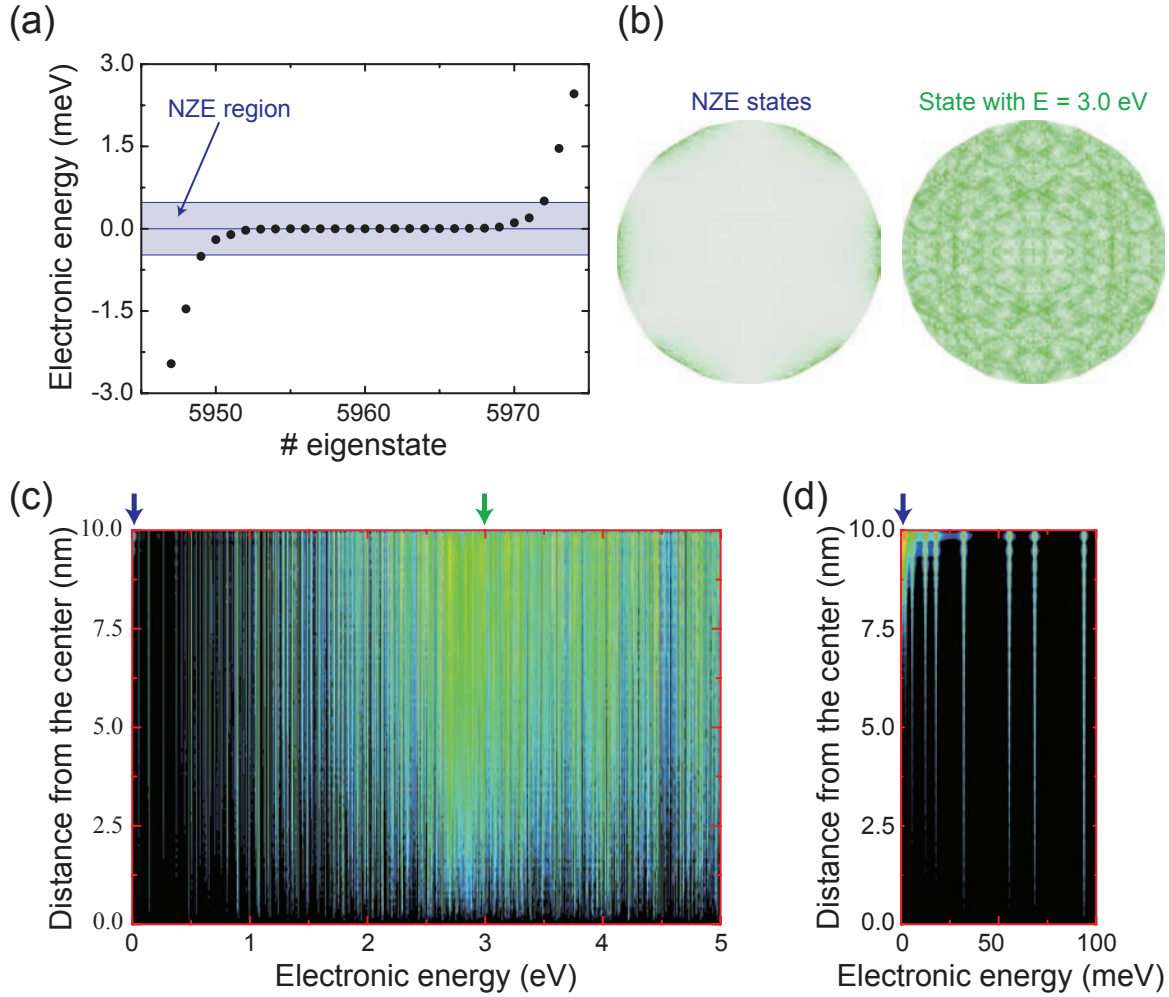


Figure S3: *Radial distribution of the tight-binding wave functions in a disk of diameter $D = 20$ nm.* (a) Energy of states piling up near zero energy (NZE). The distribution of state energies is symmetric with respect to 0 for neutral disks. (b) Spatial variation of the average probability density of states within the NZE region shown in (a) (left), and probability of a state of energy ~ 3 eV (right). (c) Radial variation of the probability density with electron energy, averaged over the disk azimuthal angle. Each electron eigenstate contributes with a vertical line to the plot, artificially broadened by a small energy width to improve readability. Only the positive-energy region is represented in the plot. (d) Zoom of the low-energy region of (c).

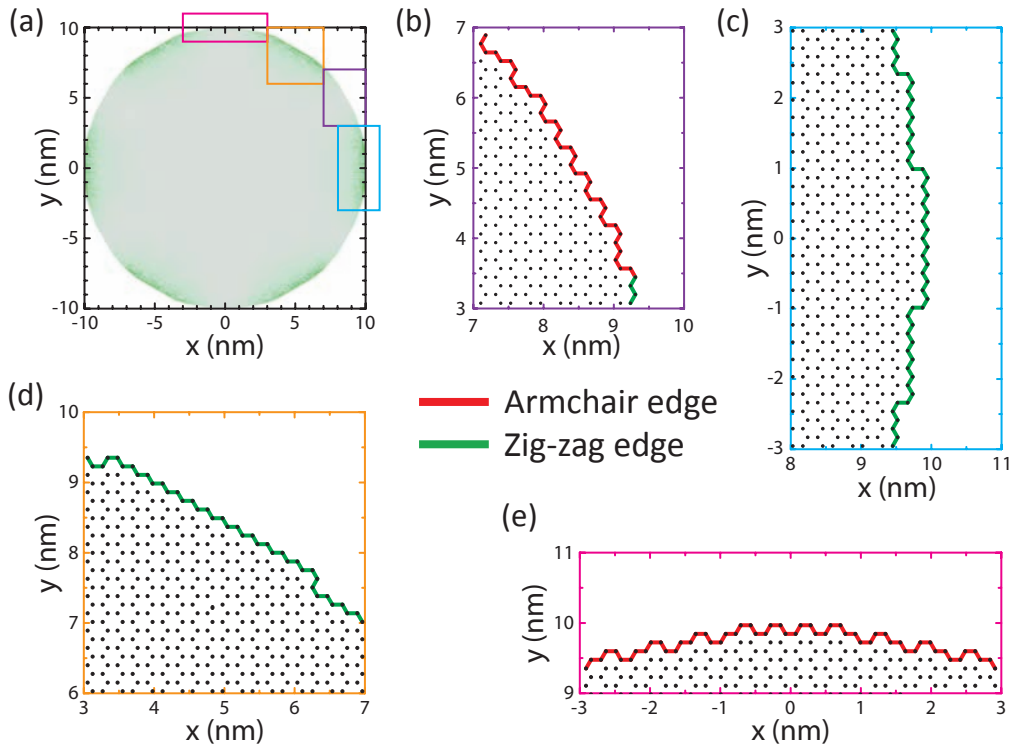


Figure S4: *Correlation of edge states with different types of graphene edges in a representative $D = 20\text{ nm}$ graphene disk.* (a) Averaged probability density of NZE states taken from Figure S3b. (b)-(e) Carbon atomic cluster near selected edge regions, zoomed from the areas indicated in (a). Higher NZE electron probability is clearly correlated with zigzag-like edges [(c) and (d)], in contrast to armchair-like edges [(b) and (e)].

can suffer modifications due to edge reconstructions, although they seem to be robust⁶ and the present description based upon unreconstructed terminations should be sufficient to explore their effects in the RPA response.

Further examination of NZE states reveals that they are mainly concentrated near zigzag-like edges (see Figure S4), which are known to support these types of modes in ribbons, in contrast to armchair-like edges.^{4,7} In particular, the state depicted in Figure S2e is concentrated in a subset of the zigzag edges, giving rise to a Fourier transform (Figure S2h) determined by the reciprocal directions of the real-space edge orientations.

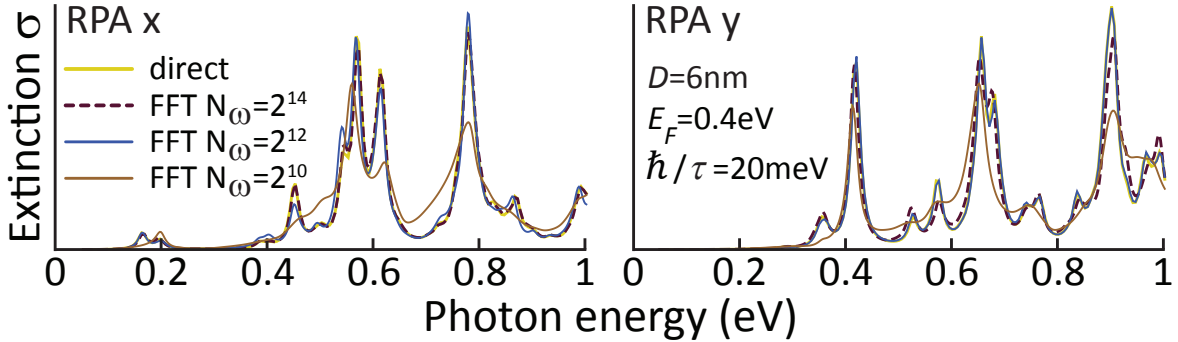


Figure S5: *Convergence of the FFT method with the number of frequencies.* Extinction cross section calculated for a disk of diameter $D = 6\text{ nm}$, Fermi energy $E_F = 0.4\text{ nm}$, and intrinsic width $\hbar\tau^{-1} = 20\text{ meV}$. The result obtained by direct summation of χ^0 is compared to the FFT evaluation of χ^0 with different numbers of frequencies N_ω . The degree of convergence is similar for polarizations along x and y directions (RPA x and RPA y , respectively).

Convergence of the FFT method used to evaluate χ^0

We show in Figure S5 that the FFT method (see Methods section in the main paper) already displays good convergence for $N_\omega = 2^{12}$ frequencies, compared to the direct evaluation of χ^0 . This degree of convergence is rather independent of the size of the structure, and therefore, we use this value of N_ω throughout the present work.

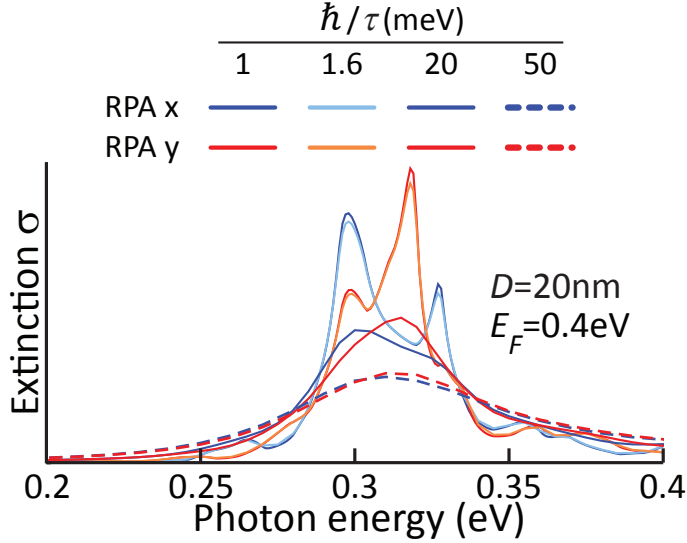


Figure S6: *Variation of extinction spectra with intrinsic relaxation time τ .* The molecular character of the response shows up through multiple narrow peaks that are clearly visible at the smallest value of $\hbar\tau^{-1}$ under consideration. These peaks broaden and eventually merge into a single peak as $\hbar\tau^{-1}$ increases.

Dependence of calculated absorption spectra on τ

In general, multiple peaks pile up near the classical plasmon energy, and their separation decreases with increasing disk size. For sufficiently large disk diameter, this separation is below the intrinsic width $\hbar\tau^{-1}$, thus leading to a single broader peak. This process, which is common to all disks under study for sizes above ~ 10 nm, is illustrated in Figure S6. Simultaneously, this emphasizes the complex nature of plasmons in graphene nanostructures, which involve a superposition of a number of collective modes that can only clearly be resolved either for artificially large values of τ or for small disks.

Strong sensitivity of absorption spectra to edge terminations

The crucial role of edge terminations in determining the spatial profile of NZE states, basically concentrated near zigzag-like edges, is translated into very different optical behavior of nanodisks depending on where their origin is placed relative to the carbon lattice. We illustrate this in Fig-

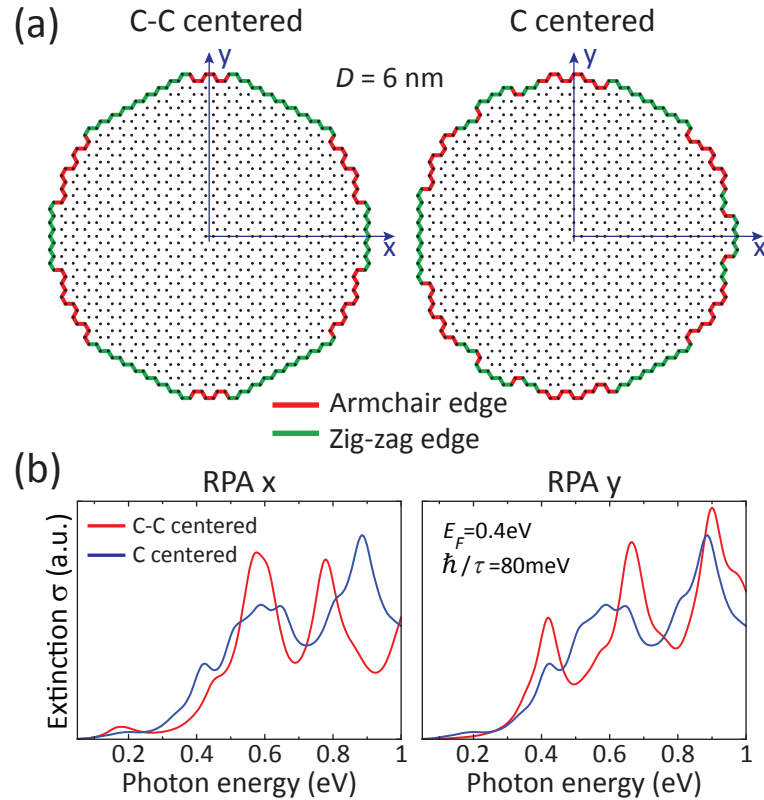


Figure S7: *Edge effects in the optical response of graphene nanodisks.* (a) Graphene disks of identical nominal diameter $D = 6\text{ nm}$ constructed as indicated in Figure S1, starting from a circumference centered either at a C-C bond (left) or at a C atom (right). These clusters display very different distributions of zigzag-like and armchair-like edges. (b) Extinction spectra calculated for x and y incident polarizations in the two clusters of (a).

ure S7 by comparing two disks of similar size (nominal diameter $D = 6\text{ nm}$) centered either at a C-C bond (C-C-centered, like in the rest of this work) or at a carbon atom (C-centered). The C-centered cluster has three-fold rotation symmetry, and therefore, its response is identical for x and y polarization directions. In contrast, the C-C-centered cluster exhibits a marked asymmetry between both of these polarization directions. The distribution of zigzag edges in these clusters is remarkably different as well (see Figure S7a), and directly affects the optical properties.

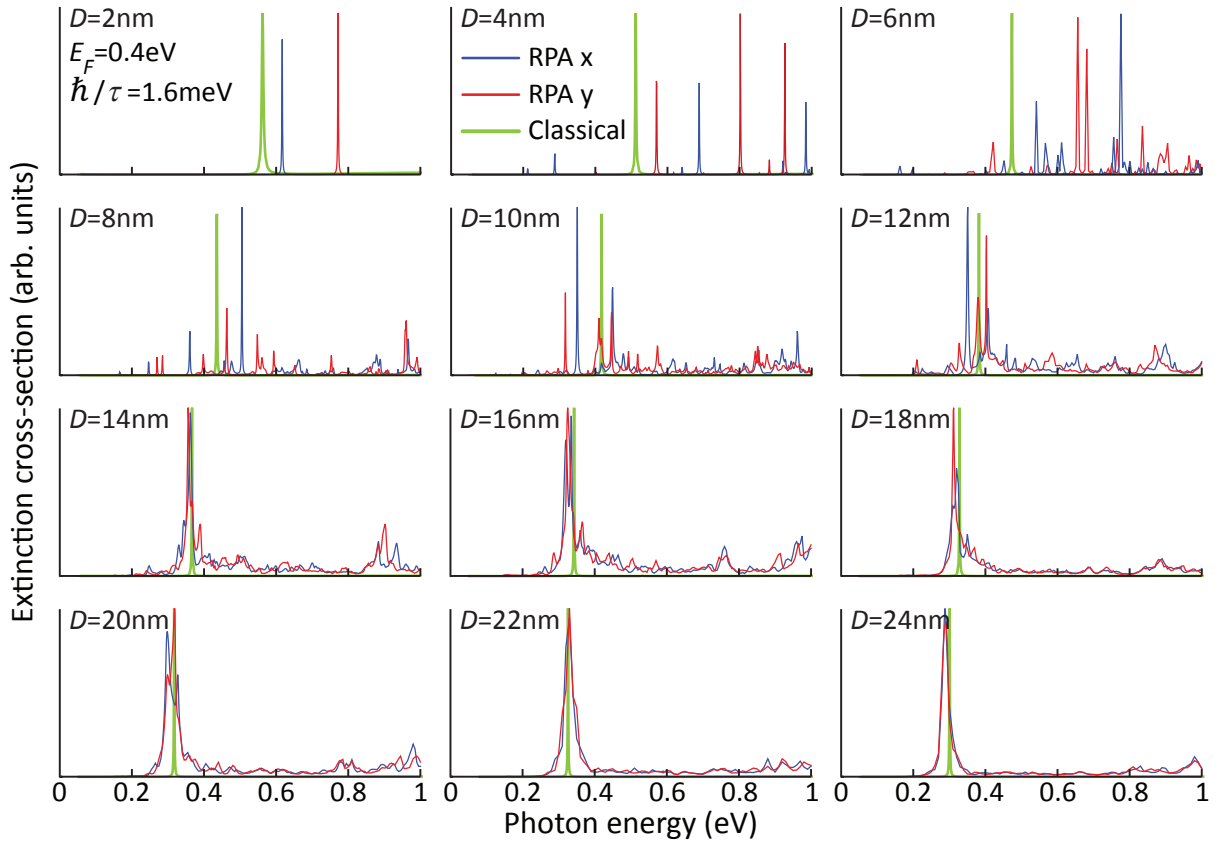


Figure S8: *Size-dependence of plasmon excitations in graphene nanodisks.* Extinction spectra of graphene disks constructed as in Figure S1 for different diameters D . The Fermi energy is $E_F = 0.4\text{ eV}$ and the intrinsic width is $\hbar\tau^{-1} = 1.6\text{ meV}$. The extinction is calculated for incident-light polarization either along x (RPA x) or y (RPA y) directions (see Figure S1). The results of classical electromagnetic calculations are shown for comparison, scaled down to improved readability.

Cluster size dependence

Nanodisks

The nanodisk size dependence of the extinction spectra is illustrated in Figure S8 for polarizations along both x and y directions parallel to the disks. Small disks show multiple peaks, which emphasize the molecular character of the structure. However, larger disks evolve towards a single in-plane dipole feature within the energy range under consideration. RPA calculations are compared to the result of a classical electromagnetic calculation. The main characteristics of these spectra are summarized in Figs. 1 and 2 of the main paper.

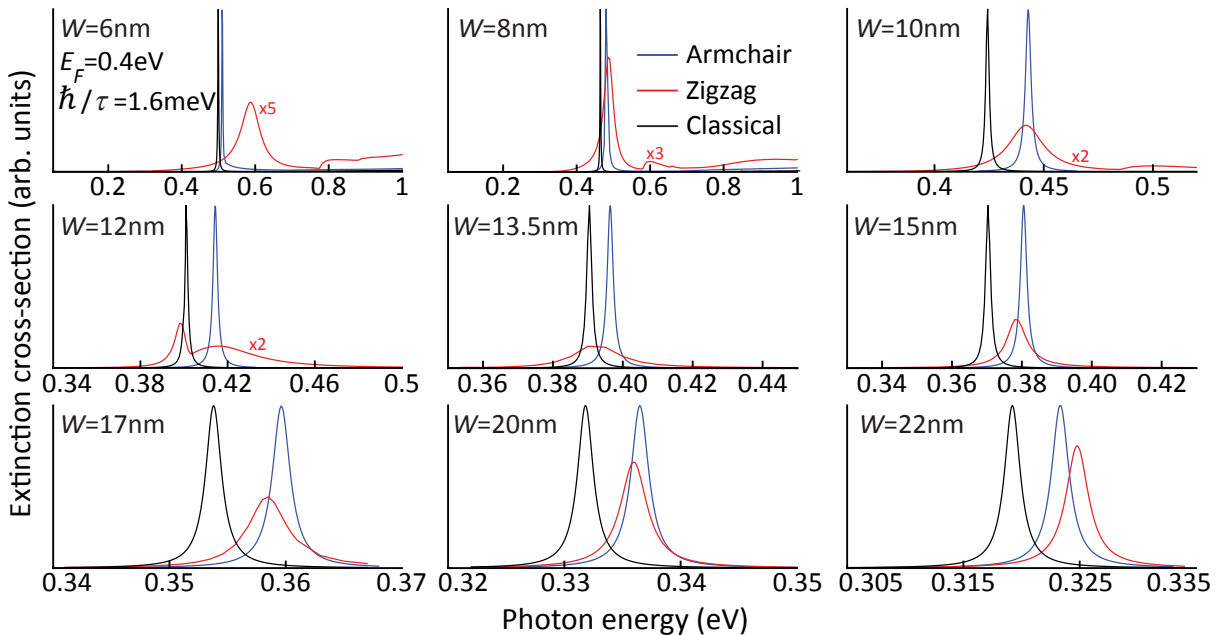


Figure S9: *Width-dependence of plasmon excitations in graphene nanoribbons.* Extinction spectra of graphene ribbons for different values of the width W . The Fermi energy is $E_F = 0.4\text{ eV}$ and the intrinsic width is $\hbar\tau^{-1} = 1.6\text{ meV}$. The extinction is calculated for light incidence perpendicular to the graphene and polarization across the ribbon width direction. Two different terminations of the graphene edges are considered: zigzag (red curves) and armchair (blue curves). The results of classical electromagnetic calculations are shown for comparison (black curves).

Nanoribbons

We show absorption spectra for ribbons of varying width and two different edge terminations in Figure S9. The relative alignment of both edges is as shown in Fig. 4a of the main paper. In contrast to nanodisks, the ribbons are essentially dominated by a single plasmon peak down to a width $W = 6\text{ nm}$. The role of edge terminations is clearly visible through additional plasmon broadening for zigzag edges compared to classical calculations. The plasmon energy and width extracted from these spectra are summarized in Fig. 4 of the main paper.

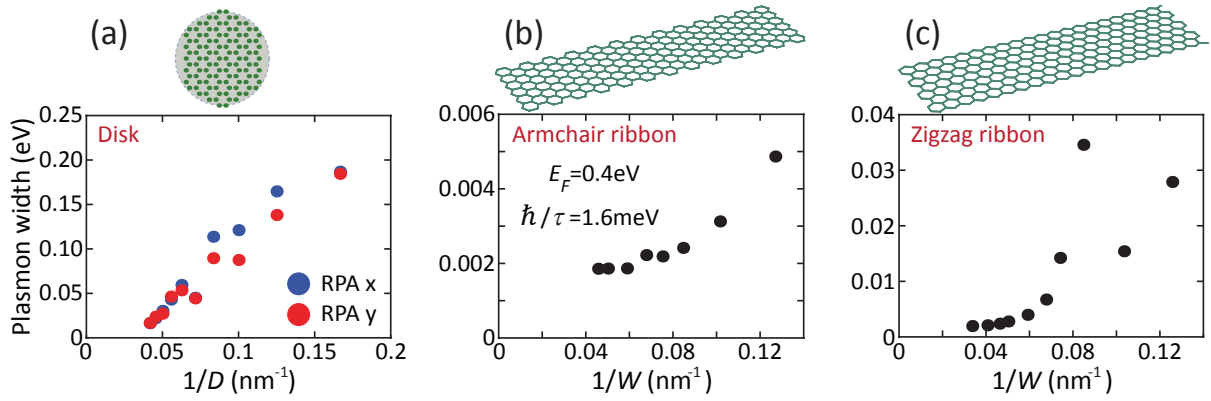


Figure S10: *Size dependence of plasmon decoherence in graphene nanodisks and nanoribbons.* (a) Dependence of the nanodisk plasmon width on the inverse diameter, $1/D$. (b,c) Plasmon width in armchair (b) and zigzag (c) nanoribbons as a function of the inverse ribbon width, $1/W$.

Plasmon decoherence

We show in Figure S10 the dependence of the plasmon width on nanodisk and nanoribbon size. The plasmon width shows a nearly linear dependence on $1/D$ in nanodisks, in contrast to a more complicated dependence on $1/W$ in nanoribbons. Furthermore, the magnitude of the plasmon width is one order of magnitude larger in nanodisks than in zigzag ribbons, and this is in turn one order of magnitude larger than in armchair ribbons. This suggests a different origin of the plasmon width in nanodisks (quantum confinement and finite-size effects) compared to ribbons (edge states in zigzag ribbons). The plasmon width in armchair ribbons, which do not support electronic edge states, is of the same order of magnitude as the intrinsic width $\hbar\tau^{-1} = 1.6\text{ meV}$.

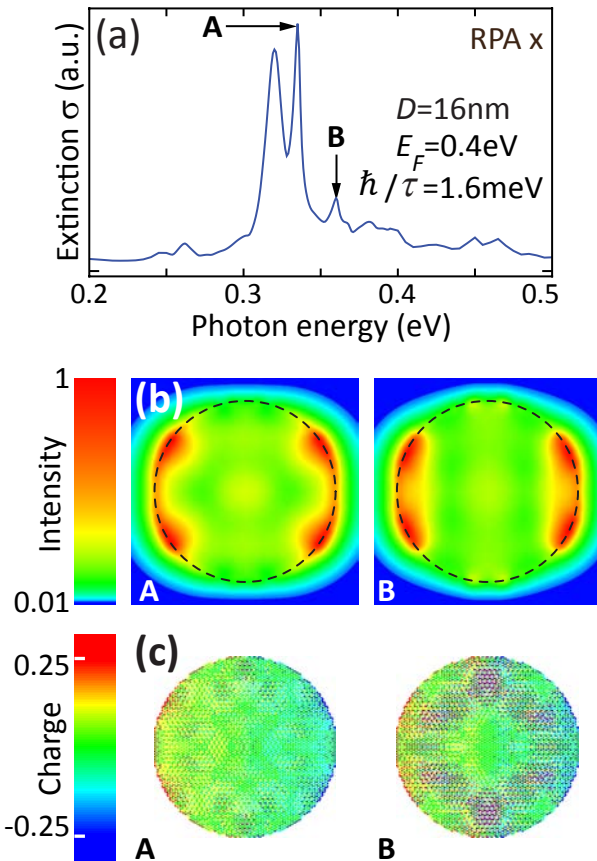


Figure S11: *Field and charge distribution associated with different peaks within the plasmonic spectral region in a graphene nanodisk.* (a) Extinction spectrum for a disk with physical parameters as shown by text insets. (b) Induced electric field intensity normalized to its maximum (log scale) and calculated at a distance of 0.5 nm above the disk for two of the spectral features indicated in (a). The intensity enhancement relative to the incident field is 598 and 55 in A and B, respectively. (c) Induced charge density amplitude normalized to its maximum (linear scale saturated outside $[-0.25, 0.25]$) for the same features as in (b). The spectral feature right to the left of A in (a) has very similar field and charge distributions as A itself.

Plasmon-peak structure

We explore in Figure S11 the complex structure of the plasmon spectral region, the multiple features of which (see discussion of Figure S6 above) are associated with very different induced field and charge distributions. Figure S11 is calculated for incident field polarization along x , and it supplements Fig. 3 of the main paper, in which we discuss results for y polarization in more detail.

Local RPA conductivity of homogeneous graphene

We use the local RPA (i.e., the limit of vanishing wave vector) for the conductivity in our classical electromagnetic calculations. This admits an analytical expression including a dependence on temperature T :⁸

$$\begin{aligned}\sigma(\omega) = & \frac{2e^2 T}{\pi \hbar} \frac{i}{\omega + i\tau^{-1}} \log [2 \cosh(E_F/2k_B T)] \\ & + \frac{e^2}{4\hbar} \left[H(\omega/2) + \frac{4i\omega}{\pi} \int_0^\infty d\varepsilon \frac{H(\varepsilon) - H(\omega/2)}{\omega^2 - 4\varepsilon^2} \right],\end{aligned}\quad (1)$$

where

$$H(\varepsilon) = \frac{\sinh(\hbar\varepsilon/k_B T)}{\cosh(E_F/k_B T) + \cosh(\hbar\varepsilon/k_B T)}.$$

The first term in Eq. (1) corresponds to intra-band transitions, in which the relaxation time has been introduced to make it converge to the Drude model at $T = 0$. The second term stands for inter-band transitions and is assumed to be independent of τ .

Convergence of electromagnetic calculations with graphene thickness

We present in Figure S12 absorption spectra calculated for graphene nanodisks using the boundary element method (BEM) with three different values of the graphene thickness t (see Meth-

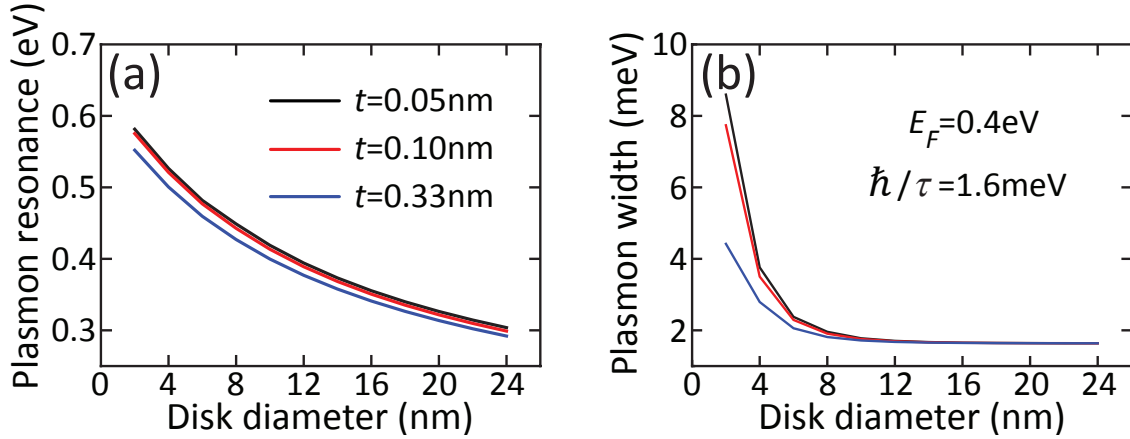


Figure S12: *Convergence of nanodisk classical calculations with graphene thickness.* Boundary-element-method (BEM) calculations for the dipolar plasmon energy (a) and width (b) of graphene nanodisks as a function disk diameter. Three different thicknesses of the graphene are examined (see labels in (a)). The Fermi energy is $E_F = 0.4\text{ eV}$ and the intrinsic width is $\hbar\tau^{-1} = 1.6\text{ meV}$ in all cases.

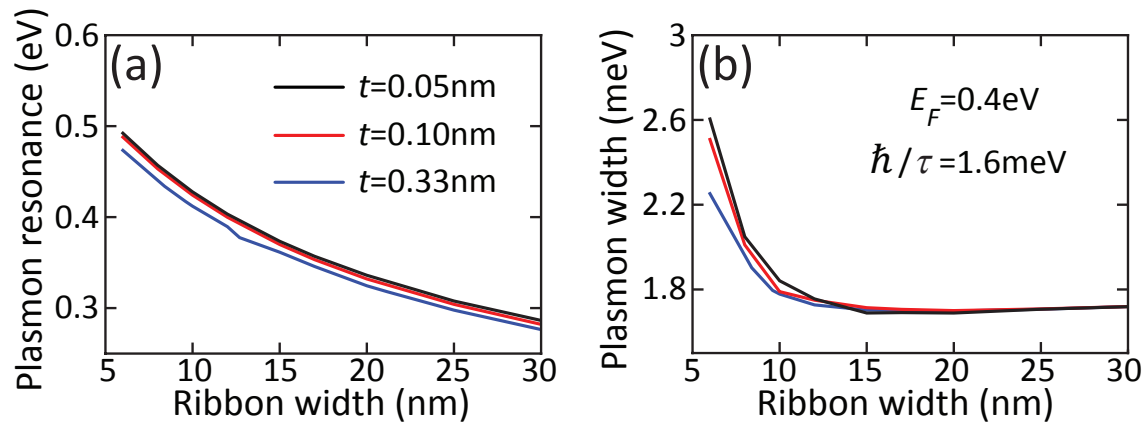


Figure S13: *Convergence of nanoribbon classical calculations with graphene thickness.* Same as Figure S12 for the dipole plasmon of graphene ribbons under normal incidence.

ods section in the main paper). The plasmon energy and width converge to well-defined values as $t \rightarrow 0$. Good convergence is already obtained for $t = 0.1$ nm, which is the value actually used in all figures of the main paper. The convergence deteriorates for small disks, particularly when examining the plasmon width, because the thickness-to-radius ratio increases and finite-thickness effects start making a significant contribution. These conclusions can be also extrapolated to ribbons, as we show in Figure S13.

References

1. Wallace, P. R. The band theory of graphite. *Phys. Rev.* **1947**, *71*, 622–634.
2. Reich, S.; Maultzsch, J.; Thomsen, C.; Ordejón, P. Tight-binding description of graphene. *Phys. Rev. B* **2002**, *66*, 035412.
3. Deacon, R. S.; Chuang, K. C.; Nicholas, R. J.; Novoselov, K. S.; Geim, A. K. Cyclotron resonance study of the electron and hole velocity in graphene monolayers. *Phys. Rev. B* **2007**, *76*, 081406(R).
4. Castro Neto, A. H.; Guinea, F.; Peres, N. M. R.; Novoselov, K. S.; Geim, A. K. The electronic properties of graphene. *Rev. Mod. Phys.* **2009**, *81*, 109–162.
5. Press, W. H.; Teukolsky, S. A.; Vetterling, W. T.; Flannery, B. P. *Numerical Recipes*; Cambridge University Press: New York, 1992.
6. Wimmer, M.; Akhmerov, A. R.; Guinea, F. Robustness of edge states in graphene quantum dots. *Phys. Rev. B* **2010**, *82*, 045409.
7. Brey, L.; Fertig, H. A. Electronic states of graphene nanoribbons studied with the Dirac equation. *Phys. Rev. B* **2006**, *73*, 235411.
8. Falkovsky, L. A.; Varlamov, A. A. Space-time dispersion of graphene conductivity. *Eur. Phys. J. B* **2007**, *56*, 281.